PHYSICAL REVIEW E VOLUME 61, NUMBER 4 APRIL 2000

Near-field diffraction tomography with diffuse photon density waves

Xingde Li,[1,2,*] Deva N. Pattanayak,[2,3] Turgut Durduran,[1] Joseph P. Culver,[1] Britton Chance,[2] and Arjun G. Yodh[1]
[1]*Department of Physics and Astronomy, University of Pennsylvania, Philadelphia, Pennsylvania 19104*
[2]*Department of Biochemistry and Biophysics, University of Pennsylvania, Philadelphia, Pennsylvania 19104*
[3]*Silicon Power Corporation, 3 Northway Lane North, Latham, New York 12110*

(Received 20 August 1999; revised manuscript received 15 December 1999)

An angular spectrum algorithm is presented for fast, near-field diffraction tomographic imaging with diffuse photon density waves in highly scattering media. A general relation in *K* space is derived that connects the spatial variations of the optical properties of heterogeneities to the spatial spectra of the measured scattered diffuse photon density waves. The theory is verified experimentally for situations when boundary effects can be neglected. We further describe how to reconstruct absorption and scattering properties simultaneously, and how to incorporate boundary conditions into this angular spectrum algorithm for a turbid medium of finite size (e.g., the slab medium). Limitations and potential improvements of the near-field diffraction tomography are also discussed.

PACS number(s): 87.10.+e, 42.25.Fx, 42.30.Wb, 42.62.Be

I. INTRODUCTION

Optical radiation was used to image breast tumors by the shadowing effect as early as the 1920s [1]. However, recent advances in light generation and detection, along with improvements in our theoretical understanding of near-infrared (NIR) light propagation in tissue-like highly scattering turbid media have opened new possibilities for optical imaging of the interior of thick biological tissues [2]. In highly scattering media such as biological tissue, light propagation is described adequately within the diffusion model of photon transport [3–5]. It has been shown by several investigators that diffuse photon density waves, which are created inside highly scattering media by an intensity modulated light source, obey a Helmholtz wave equation with a complex wave number [6,7]. In spite of complexities resulting from strong tissue scattering, diffusing photons offer many attractive features for imaging thick tissue. These features include noninvasiveness, low cost, and unique optical contrast and spectroscopic signatures with clinical and physiological relevance [8,9].

The goal of diffuse optical imaging is to reconstruct a low resolution map of heterogeneous absorption and scattering variations from the measurements of diffuse photons on a sample surface. Image reconstruction entails solving the inverse problem. Most quantitative optical image reconstruction algorithms such as the algebraic reconstruction technique (ART), the simultaneous iterative reconstruction technique (SIRT) [10], the Newton-Raphson technique combined with finite element numerical method [11–13], the conjugate gradient descent technique [14], and singular value decomposition (SVD) [15], rely on iterative schemes in a least-square sense. The optical image reconstruction therefore requires a significant amount of computational resources and time.

Recently, we showed that by using the techniques of diffraction tomography [16,17], it is possible to rapidly reconstruct thin slice and spherical objects whose absorption and/or scattering parameters differ from the background homogeneous scattering medium [20]. Our image reconstruction algorithm, based upon diffraction tomography technique (called angular spectrum algorithm in this paper), is rapid, permitting object localization and characterization in ~1000 volume-element samples on sub-second computational time scales. Such an angular spectrum algorithm has recently attracted the attention of many researchers in photon migration field [18,19]. In this paper we provide a more complete discussion of the results reported in those earlier papers, and we provide a detailed analysis of this algorithm incorporating the effects of finite boundaries. We first derive the general integral solution of the total and scattered photon density waves in a heterogeneous turbid medium within the first order Born approximation (Secs. II, III, and IV). These sessions are largely reviews, but are included for completeness and clarity. We next derive a relation in *K* space between the spatial spectrum of the heterogeneity function and the spatial spectrum of the measured scattered diffuse photon density wave (Sec. V A). Experimental results are presented to verify the feasibility of the angular spectrum algorithm for image reconstruction. We then describe a method to reconstruct the absorption and scattering properties simultaneously with this algorithm. Some limitations and potential improvements of the diffraction tomography are discussed in Sec. VI. Finally, we illustrate how to incorporate boundary conditions into the angular spectrum algorithm for a turbid medium of finite size, in particular, the slab medium and the semi-infinite medium (Sec. VII).

II. PHOTON DIFFUSION EQUATION IN HETEROGENEOUS MEDIA–A PERTURBATION APPROACH

Light transport in highly scattering turbid media is often well described by photon diffusion [2]. Consider a light source at $\mathbf{r_s}$ with its intensity sinusoidally modulated at modulation frequency f, e.g., the source term is $S(\mathbf{r},t)$

---

[*] Present address: Department of Electrical Engineering and Computer Science, Massachusetts Institute of Technology, Cambridge, MA 02139. Electronic address: xingde@mit.edu

1063-651X/2000/61(4)/4295(15)/$15.00

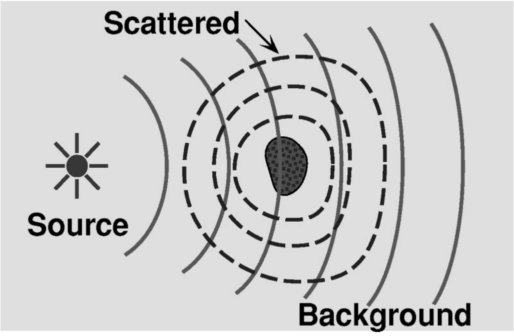

FIG. 1. In the presence of optical inhomogeneities, the spherical wave fronts of the background wave are distorted and the scattered wave is generated. The total photon density wave is the sum of the background wave and the scattered wave.

$=S(\mathbf{r})e^{-i\omega t}=M_0e^{-i\omega t}\delta(\mathbf{r}-\mathbf{r_s})$, where $\omega=2\pi f$ is the angular source modulation frequency,[1] M_0 is the source strength representing the number of photons emitted per second. Consider steady-state photon diffusion in which the photon fluence $\Phi(\mathbf{r},t)$ has the same time dependence as the source, i.e., $\Phi(\mathbf{r},t)=\Phi(\mathbf{r})e^{-i\omega t}$. It is straight forward to show that the photon fluence $\Phi(\mathbf{r})$ satisfies the photon diffusion equation [3–5]:

$$\nabla\cdot(D\nabla\Phi(\mathbf{r}))-v\mu_a\Phi(\mathbf{r})+i\omega\Phi(\mathbf{r})=-vS(\mathbf{r}). \tag{1}$$

Here the common time dependence $\exp(-i\omega t)$ of the fluence $\Phi(\mathbf{r})$ and the source $S(\mathbf{r})$ are omitted. v is the speed of light in the turbid medium; $D=v/3\mu_s'$ is photon diffusion coefficient; μ_a and μ_s' are respectively the optical absorption and reduced scattering coefficients.

In a homogeneous medium, the absorption and scattering coefficients (μ_{a0} and μ_{s0}') are constant, and the above equation reduces to a simple Helmholtz equation:

$$(\nabla^2+k_0^2)\Phi_0(\mathbf{r})=-3\mu_{s0}'S(\mathbf{r}). \tag{2}$$

Here the wave number k_0 is complex and $k_0=[3\mu_{s0}'(-\mu_{a0}+i\omega/v)]^{1/2}$ with $\mathrm{Im}(k_0)>0$ to ensure that the photon density goes to zero at a large distance.

In an optically heterogeneous turbid medium, the spherical wave fronts of the background wave are distorted by inhomogeneities. As illustrated in Fig. 1, the total photon density wave $\Phi(\mathbf{r})$ is the sum of the background wave $\Phi_0(\mathbf{r})$ and the scattered wave $\Phi_{sc}(\mathbf{r})$

$$\Phi(\mathbf{r})=\Phi_0(\mathbf{r})+\Phi_{sc}(\mathbf{r}). \tag{3}$$

The background wave $\Phi_0(\mathbf{r})$ represents the photon density wave in a homogeneous turbid medium for an arbitrary geometry; the scattered wave is produced by optical inhomogeneities in an otherwise homogeneous medium with the same geometry as the background wave. The scattered wave is determined by characteristics of the inhomogeneity such as its size, shape, position, and its absorption and scattering properties. The goal of optical tomography is to reconstruct the map of these heterogeneous optical properties from measurements of the scattered wave.

In a heterogeneous medium we write the optical properties (μ_a and μ_s') as the sum of background optical properties (μ_{a0}, μ_{s0}') and the variations relative to the background ($\delta\mu_a$, $\delta\mu_s'$), i.e.,

$$\mu_a(\mathbf{r})=\mu_{a0}+\delta\mu_a(\mathbf{r}), \tag{4}$$

$$\mu_s'(\mathbf{r})=\mu_{s0}'+\delta\mu_s'(\mathbf{r}). \tag{5}$$

Consider the case of weak optical inhomogeneities where $\delta\mu_a\ll\mu_{a0}$ and $\delta\mu_s'\ll\mu_{s0}'$. The optical inhomogeneities introduce a weak perturbation to the background wave, i.e., $|\Phi_{sc}(\mathbf{r})|\ll|\Phi_0(\mathbf{r})|$. Substituting Eqs. (4) and (5) into Eq. (1) and keeping only the zeroth and first order terms in optical property variations as well as in the scattered wave, we find

$$(\nabla^2+k_0^2)\Phi(\mathbf{r})=-\frac{v}{D_0}\left[1+\frac{\delta\mu_s'(\mathbf{r})}{\mu_{s0}'}\right]S(\mathbf{r})-T_{abs}(\mathbf{r})-T_{sc}(\mathbf{r}), \tag{6}$$

where we have introduced the heterogeneity functions $T_{abs}(\mathbf{r})$ and $T_{sc}(\mathbf{r})$ representing the perturbations due to the absorption and scattering variations. They are

$$T_{abs}(\mathbf{r})=-\frac{v}{D_0}\Phi_0(\mathbf{r})\delta\mu_a(\mathbf{r}), \tag{7}$$

$$T_{sc}(\mathbf{r})=\frac{3D_0k_0^2}{v}\Phi_0(\mathbf{r})\delta\mu_s'(\mathbf{r})-\frac{\nabla[\delta\mu_s'(\mathbf{r})]}{\mu_{s0}'}\cdot\nabla\Phi_0(\mathbf{r}). \tag{8}$$

Note that $\delta\mu_s'(\mathbf{r})/\mu_{s0}'S(\mathbf{r})$ is zero as long as the source is outside the inhomogeneity (which is generally the case in practice), and therefore we can drop this term from Eq. (6). In addition we assume, for simplicity, that the scattering varies slowly in space so that the term $\nabla[\mu_{s0}'+\delta\mu_s'(\mathbf{r})]/\mu_{s0}'\cdot\nabla\Phi_0(\mathbf{r})$ can be neglected. We thus have the following simplified equation for the total photon density wave $\Phi(\mathbf{r})$ within the first order Born approximation

$$(\nabla^2+k_0^2)\Phi(\mathbf{r})=-\frac{v}{D_0}S(\mathbf{r})-T(\mathbf{r}), \tag{9}$$

where $T(\mathbf{r})=T_{abs}(\mathbf{r})+T_{sc}(\mathbf{r})$ and the heterogeneity functions $T_{abs}(\mathbf{r})$ and $T_{sc}(\mathbf{r})$ are given by

$$T_{abs}(\mathbf{r})=-\frac{v}{D_0}\Phi_0(\mathbf{r})\delta\mu_a(\mathbf{r}) \tag{10}$$

$$T_{sc}(\mathbf{r})=\frac{3D_0k_0^2}{v}\Phi_0(\mathbf{r})\delta\mu_s'(\mathbf{r}). \tag{11}$$

We see that the heterogeneity functions can be treated as equivalent ''source'' terms, which give rise to the scattered component $\Phi_{sc}(\mathbf{r})$ of the total diffuse photon density wave $\Phi(\mathbf{r})$.

---

[1] The continuous-wave (CW) case is a special case where $\omega=0$ and the frequency domain analysis can be readily applied to the CW case.

III. TOTAL DIFFUSE PHOTON DENSITY WAVE IN HETEROGENEOUS TURBID MEDIA — THE GREEN'S FUNCTION APPROACH

We will take a Green's function approach to derive the total and therefore the scattered photon density wave in a heterogeneous highly scattering medium. Consider the Green's function in turbid media which satisfies

$$(\nabla^2+k_0^2)G(\mathbf{r},\mathbf{r}')=-\delta(\mathbf{r},\mathbf{r}'). \qquad (12)$$

Using the Green's theorem, we obtain an integral expression for the total optical density wave $\Phi(\mathbf{r})$

$$\Phi(\mathbf{r})=\frac{v}{D_0}\int_V S(\mathbf{r}')G(\mathbf{r},\mathbf{r}')d^3r'+\int_V T(\mathbf{r}')G(\mathbf{r},\mathbf{r}')d^3r' + \int_S\left[G(\mathbf{r},\mathbf{r}')\frac{\partial\Phi(\mathbf{r}')}{\partial n'}-\Phi(r')\frac{\partial G(\mathbf{r},\mathbf{r}')}{\partial n'}\right]dA'. \qquad (13)$$

The first term on the right-hand side of Eq. (13) is a volume integral of the light source over the entire turbid medium. It gives us the background wave. The second term is a volume integral of the heterogeneity function over the entire turbid medium and it determines the perturbation resulting from the optical heterogeneities. The third term is a surface integral over the closed surface of the entire turbid medium. It takes into account the boundary effects on the total photon density wave, and it includes contributions to the total photon density wave from both the background wave and the scattered wave on the boundary. n' in the surface term denotes the surface normal pointing outward. For an infinite heterogeneous medium, this surface term is zero since the enclosure surface of an infinite medium is at infinity. Therefore the scattered wave can be simply separated from the background wave. For a finite turbid medium, however the separation of the background wave component from the scattered wave component in the surface term is generally difficult. It is advantageous therefore to remove the surface integral from the total photon density wave by choosing an appropriate Green's function. We will consider this complicated (yet more realistic) case at the end of this paper. We will start with a simple case - the infinite geometry case.

IV. SCATTERED WAVE IN INFINITE HETEROGENEOUS TURBID MEDIA

As shown in Fig. 1, in the presence of optical heterogeneities, the total photon density wave consists of the background wave and the scattered wave, and the scattered wave carries the information of the optical inhomogeneities. For an infinite geometry, the surface integral in Eq. (13) disappears. The background wave in this case is given by the first term (volume integral of the source) on the right-hand side of Eq. (13). For an infinite geometry, the Green's function is $G_0(\mathbf{r},\mathbf{r}')=\exp(ik_0|\mathbf{r}-\mathbf{r}'|)/4\pi|\mathbf{r}-\mathbf{r}'|$. Using this Green's function and considering a point source at $\mathbf{r_s}$, i.e., $S(\mathbf{r}')=M_0\delta(\mathbf{r}'-\mathbf{r_s})$, we can readily show that the scattered wave [by definition: the difference between the total photon density wave $\Phi(\mathbf{r})$ and the background wave $\Phi_0(\mathbf{r})$] is

$$\Phi_{sc}(\mathbf{r})=\Phi(\mathbf{r})-\Phi_0(\mathbf{r})=\int_V T(\mathbf{r}')G_0(\mathbf{r},\mathbf{r}')d^3r'. \qquad (14)$$

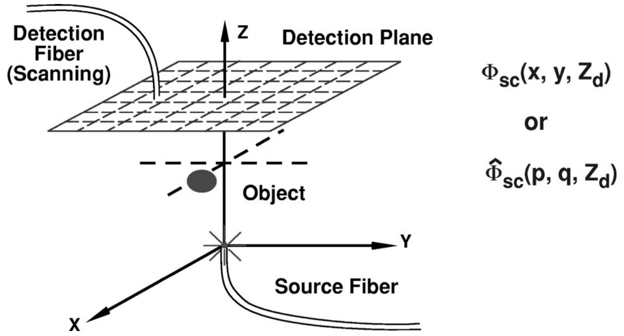

FIG. 2. Illustration of 2D geometry which we consider for the image reconstruction algorithm based upon *K*-space spectrum analysis. The scattered wave $\Phi_{sc}(x,y,z_d)$ (or its spatial Fourier component $\hat{\Phi}_{sc}(p,q,z_d)$ is determined at the detection plane $z=z_d$ by scanning the detector over a square region. Without losing generality we assume the optical heterogeneities are located below the detection plane at $z=z_d$. A point source can be placed anywhere in the turbid medium. In practice the point source and the detection plane are either on the opposite side of the heterogeneities (transmission) or both on the same side of the heterogeneities (re-emission). In this figure the point source happens to be placed at the origin of our coordinate system for demonstration of a transmission measurement geometry.

V. IMAGE RECONSTRUCTION ALGORITHM AND EXPERIMENTAL RESULTS

The scattered wave depends on the heterogeneity function. In practice the scattered wave can be obtained from measurements and knowledge of the background wave. Given the scattered wave, how can one obtain the heterogeneity function and thus $\delta\mu_a(\mathbf{r})$ and $\delta\mu_s'(\mathbf{r})$? The approach we take here employs the angular spectrum analysis of the scattered wave. In this approach we relate the spatial spectrum of the scattered wave to the spatial spectrum of the heterogeneity function. The analysis involves forward and inverse Fourier transforms following the conventions given in Appendix A.

A. The angular spectrum algorithm

The experiment we consider for the angular spectrum algorithm has a two-dimensional (2D) planar geometry. As shown in Fig. 2, the scattered wave $\Phi_{sc}(\mathbf{r})$ is determined at a plane $z=z_d$ from a set of measurements in that plane. Equation (14) tells us that the scattered wave $\Phi_{sc}(\mathbf{r})$ is the convolution of the heterogeneity function $T(\mathbf{r})$ with the Green's function $G_0(\mathbf{r},\mathbf{r}')$. In order to reveal the relation between the scattered wave and the heterogeneity function in *K* space, we first expand the Green's function in terms of plane waves in two dimensions, i.e.,

$$G_0(\mathbf{r}_d,\mathbf{r}')=\int_{-\infty}^{+\infty}\int dpdq\hat{G}_0(p,q,z_d,z')e^{-i2\pi[p(x_d-x')+q(y_d-y')]}=\int_{-\infty}^{+\infty}\int dpdq\frac{i}{2m}e^{im|z_d-z'|}e^{-i2\pi[p(x_d-x')+q(y_d-y')]},\tag{15}$$

where (p,q) are the 2D spatial frequencies with respect to the x-y coordinates. In the second line of the above equation, we have employed the Weyl expansion of the Green's function [21], i.e.,

$$\hat{G}_0(p,q,z_d,z')=\frac{i}{2m}e^{im|z_d-z'|},\tag{16}$$

where $m=[k_0^2-(2\pi)^2(p^2+q^2)]^{1/2}$ and $\mathrm{Im}(m)>0$. The derivation of the Weyl expansion of the Green's function is given in Appendix B.

Note that Eq. (15) is the *angular spectrum* representation of the Green's function, a solution of the wave equation with a point source at (x',y',z'). At any point inside the half space to the right (or left) of the source, there are eigen-plane waves in the x-y plane whose amplitudes and phases vary with the distance from the source $|z_d-z'|$. Because of the large positive imaginary part of m, the amplitude decays exponentially versus the perpendicular distance $|z_d-z'|$ away from the source point. Plane waves with large spatial frequencies (p,q) (and therefore a large imaginary part of m) will have negligible amplitudes. This is the characteristic difference between diffuse photon density waves and ordinary diffractive electromagnetic waves in lossless dielectric media. These plane waves will be scattered by optical inhomogeneities and their resulting amplitudes and phases will carry information about the absorption and/or scattering characteristics of the inhomogeneities.

If we substitute the angular spectrum representation of the Green's function [Eq. (15)] into the volume integral of the scattered wave given by Eq. (14), after simple algebraic manipulation and interchanging the order of integrations, we obtain the following representation, known as the *angular spectrum* representation of the scattered wave

$$\Phi_{sc}(\mathbf{r}_d)=\int\int_{-\infty}^{+\infty}dpdqe^{-i2\pi(px_d+qy_d)}\times\int dz'\hat{G}_0(p,q,z_d,z')\hat{T}(p,q,z'),\tag{17}$$

where $\hat{T}(p,q,z')$ is the 2D spatial spectrum (Fourier transform) of the heterogeneity function, i.e.,

$$\hat{T}(p,q,z')=\int\int_{-\infty}^{+\infty}dx'dy'T(x',y',z')e^{i2\pi(px'+qy')}.\tag{18}$$

Taking the 2D Fourier transform of the scattered wave $\Phi_{sc}(\mathbf{r}_d)$ in the detection plane at $z=z_d$, i.e.,

$$\Phi_{sc}(\mathbf{r}_d)=\int\int_{-\infty}^{+\infty}dpdq\hat{\Phi}_{sc}(p,q,z_d)e^{-i2\pi(px_d+qy_d)},\tag{19}$$

and comparing Eq. (17) and Eq. (19), we then obtain the relation between the spatial spectrum of the scattered wave and the spatial spectrum of the heterogeneity function at any given spatial frequency (p,q), i.e.,

$$\hat{\Phi}_{sc}(p,q,z_d)=\int_{-\infty}^{\infty}dz'\hat{G}_0(p,q,z_d,z')\hat{T}(p,q,z').\tag{20}$$

Without losing generality, we assume the optical heterogeneities are *below* the detection plane. This assumption enables us to remove the absolute value sign in the Weyl expansion in Eq. (16) since $z_d-z'>0$. We also assume the heterogeneities are localized between the detection plane at $z=z_d$ and a plane at $z=z_0$. Thus we need consider only the interval between $(z=z_0,\ z=z_d)$ for the integral in Eq. (20). Dividing the turbid medium between the plane at $z=z_0$ and the detection plane into slices, we can rewrite Eq. (20) in the following form of discretized summation

$$\hat{\Phi}_{sc}(p,q,z_d)=\sum_{j=1}^{N}\Delta z\hat{T}(p,q,z_j)\hat{G}_0(p,q,z_d,z_j)=\sum_{j=1}^{N}\frac{i\Delta z}{2m}\hat{T}(p,q,z_j)e^{im(z_d-z_j)},\tag{21}$$

where in the second line we substitute the Green's function $\hat{G}_0(p,q,z_d,z_j)$ with its Weyl expansion [Eq. (16)]; Δz is the discretized step size along the z direction and N is the total number of slices in the z direction. Ideally the discretization step size Δz needs to be as small as possible. In practice we choose Δz to be a few random walk steps (i.e., $\sim 1/\mu_s'$).

Equation (21) implies that at any given spatial frequency (p,q), the heterogeneity functions at different depth z_j's can be thought of as the ''source terms'' for the scattered wave. The plane waves arising from different slices propagate along the z direction to the detection plane. During the propagation these plane waves experience different amplitude attenuation and phase shifts which are given by $e^{im(z_d-z_j)}/m$, where $m=[k_0^2-(2\pi)^2(p^2+q^2)]^{1/2}$ is a complex number with $\mathrm{Im}(m)>0$; the scattered wave detected at the detection plane $z=z_d$ is thus a sum of plane waves originating from the heterogeneity functions at different depths. In Fig. 3 we illustrate this concept. In this figure we consider two nonzero heterogeneity functions $\hat{T}_1(p,q=0,z_1)$ and $\hat{T}_2(p,q=0,z_2)$ corresponding to plane waves along the x direction in the x-z plane (i.e., $y=0$) with a spatial frequency p at depth z_1 and z_2. The perturbations from these two slices propagate to the detection plane with a phase shift and amplitude attenuation factor $e^{im(z_d-z_j)}/m$. At the detection plane the perturbations from these two slices add up to make a scattered wave $\hat{\Phi}_{sc}(p,q=0,z_d)$ at the same spatial frequency p.

In K space the propagation of the perturbation $\hat{T}(p,q,z_j)$ at different depths z_d-z_j is weighted by the amplitude attenuation and phase shift given by the Weyl expansion of the Green's function $\hat{G}_0(p,q,z_d,z_j)=ie^{im(z_d-z_j)}/(2m)$. Recall

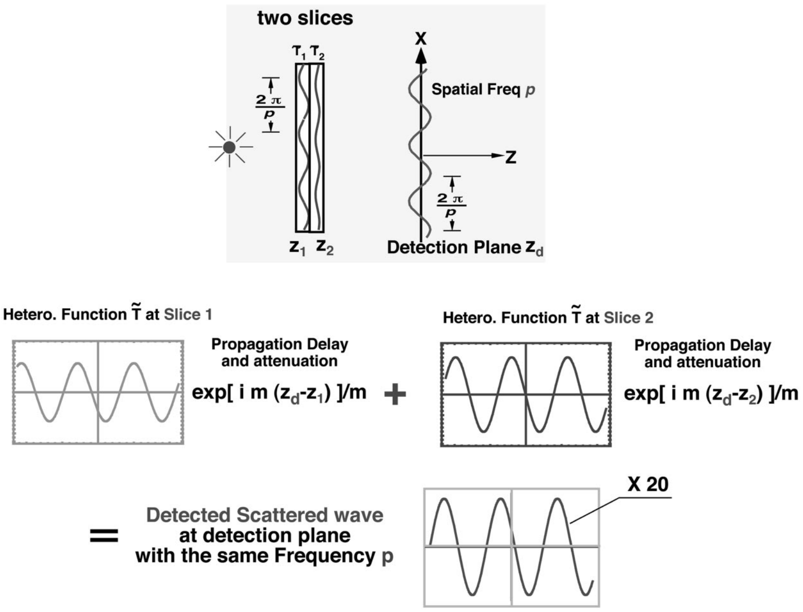

FIG. 3. The heterogeneity functions $\hat{T}_1$ and $\hat{T}_2$ with spatial frequency *p* from two slices propagate to the detection plane at $z=z_d$ where they add up to make the scattered wave $\hat{\Phi}_{sc}$ in *K* space at the same spatial frequency *p*.

$m=[k_0^2-(2\pi)^2(p^2+q^2)]^{1/2}$ with $\mathrm{Im}(m)>0$, therefore the amplitude and phase of the Weyl expansion $\hat{G}_0(p,q,z_d,z_j)$ depend on the spatial frequency (p,q) at a given depth z_d-z_j. The amplitude decays more quickly as the spatial frequencies (p,q) increase, and the Green's function effectively acts as a low pass filter in *K* space.

For spatial frequencies (p,q) with the range of (0, 1.6) cm^{-1}, we plot the amplitude and phase of the Weyl expansion ($\sim e^{im(z_d-z_j)}/m$) in Figs. 4(a) and 4(b) assuming the depth is $z_d-z_j=1$ cm. In calculating the background diffuse wave wave number $k_0=[(-v\mu_{a0}+i\omega)/D_0]^{1/2}$ we choose background optical properties $\mu_{a0}=0.02$ cm^{-1} and

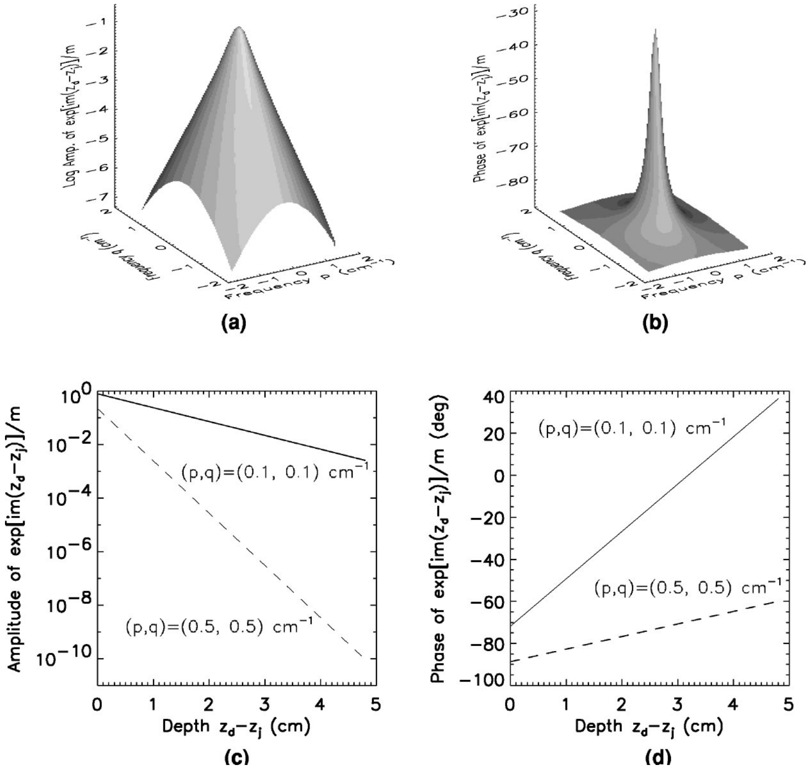

FIG. 4. (a) and (b) respectively show the amplitude attenuation and phase shift associated with the Weyl expansion in *K* space versus spatial frequencies (p,q). Note in (a) the *z* axis is the log of the amplitude of $e^{im(z_d-z_j)}/m$; in (b) the *z* axis is the phase of $e^{im(z_d-z_j)}/m$ in degrees. (c) and (d) show the amplitude attenuation and phase shift versus the depth z_d-z_j for given spatial frequencies (0.1, 0.1) cm^{-1} (solid lines) and (0.5, 0.5) cm^{-1} (dashed lines).

$\mu'_{s0} = 8.0\ \text{cm}^{-1}$, and a 140 MHz modulation frequency. The resultant wave number is $|k_0| \sim 1.1\ \text{cm}^{-1}$. We find that the amplitude attenuates by ~ 7 orders of magnitude when the spatial frequencies (p,q) increase from (0, 0) cm^{-1} to (1.6, 1.6) cm^{-1}. In practice the maximum spatial frequency is determined by the Nyquist sampling frequency, i.e., $q_{max} = 1/2\Delta x \approx 0.833\ \text{cm}^{-1}$ for a scanning step size $\Delta x = 0.6$ cm. In Figs. 4(c) and 4(d), we also plot the amplitude attenuation and phase shift versus depth for given spatial frequencies, i.e., (0.1, 0.1) cm^{-1} and (0.5, 0.5) cm^{-1}. The amplitude attenuates exponentially and the phase shift increases linearly as we consider the perturbation from deeper slices. Again as already shown in Fig. 4(c), the amplitude attenuates much faster at spatial frequencies (0.5, 0.5) cm^{-1} than at (0.1, 0.1) cm^{-1}. At any given depth $(z_d - z_j)$, those plane waves with sufficiently large spatial frequencies (p,q) have negligible contribution to the scattered wave, and therefore carry less information about the inhomogeneities.

B. 2D projection imaging

2D photographic images have been used by radiologists for many years. In order to acquire 2D photographic-type *projection* images, we make a ''thin'' slice approximation by replacing z_j on the left hand side of Eq. (21) with the estimated slice position of the object. We then drop the sum over all *other* z_j's and obtain the following simple relation at any given spatial frequency (p,q) in K space between the heterogeneity function at depth $z = z_{obj}$ and the measured scattered wave at the detection plane $z = z_d$:

$$\hat{T}(p,q,z_{obj}) = \frac{\hat{\Phi}_{sc}(p,q,z_d)}{\Delta z \hat{G}_0(p,q,z_d,z_{obj})} = \frac{2m}{i\Delta z}\hat{\Phi}_{sc}(p,q,z_d)e^{-im(z_d - z_{obj})}. \qquad (22)$$

This ''thin'' slice approximation may be adequate since we are often interested in early tumors whose size will be of the order of slice thickness of ~ 0.5 cm, and thus can be considered thin. As we discussed at the end of Sec. V(A), plane waves in K space with large spatial frequencies (p,q) are attenuated quickly as they propagate within the turbid media. The largest detectable spatial frequencies are determined by the sensitivity and signal-to-noise ratio of the detection system.

When the heterogeneity function in K space, $\hat{T}(p,q,z_{obj})$, is determined by Eq. (22), we can then take the inverse 2D Fourier transform of $\hat{T}(p,q,z_{obj})$ to obtain the tumor function $T(x,y,z_{obj})$ in the real x-y space at the depth of the heterogeneity $z = z_{obj}$. We derive a 2D photographic image of the optical properties using Eqs. (10) and (11); for example, $\delta\mu_a(x,y,z_{obj}) = T_{abs}(x,y,z_{obj})/[-v/D_0\Phi_0(x,y,z_{obj})]$ for absorbing objects, and $\delta\mu'_s(x,y,z_{obj}) = T_{sc}(x,y,z_{obj})/[3D_0k_0^2/v\Phi_0(x,y,z_{obj})]$ for scattering objects. Note that for a purely absorbing or scattering object, either a frequency domain (modulation frequency $f \neq 0$) or a continuous-wave (CW, $f = 0$) DPDW can be employed to extract the absorption or scattering variation; but for objects having both absorption and scattering variations, a CW DPDW is not sufficient to separate the absorption and scattering [see Sec. VI(A)].

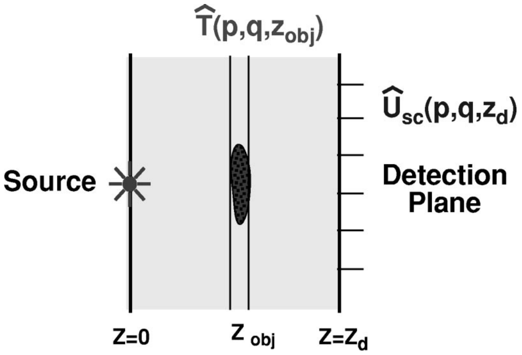

FIG. 5. The heterogeneities are considered to be thin, which locate within a thin slice at $z = z_{obj}$ in parallel to the detection plane. The heterogeneity function within this thin slice is approximately uniform and the heterogeneity function is zero elsewhere.

Consider next a case where the optical heterogeneities are located within a ''thin'' slice at $z = z_{obj}$ (see Fig. 5). If the slice thickness Δz is less than a few transport mean free path-lengths $[1/(\mu'_{s0} + \mu_{a0})]$, the heterogeneity function within this thin slice is approximately uniform, therefore Eq. (22) provides a quite accurate relation between the heterogeneity function and the scattered wave in K space, and optical properties of the heterogeneity can further be deduced quite accurately. For thicker objects (i.e., thickness > 4 mm), the average over the size of the object weighted by the sum of exponential amplitude and phase factors $e^{im(z_d - z_j)}/m$ provides only an approximate relation between the heterogeneity function and the scattered wave. However we find that the relative optical properties of multiple objects can still be reconstructed with an reasonable accuracy.

Obviously the image reconstruction involves only 2D forward and inverse Fourier transforms, and no iterative schemes are needed; therefore this angular spectrum algorithm is very rapid.

C. *A priori* depth information and perspectives of 3D imaging

From the derivation we notice that in principle, this K-space spectrum analysis algorithm should work well when the optical heterogeneities are confined within a thin slice. The reconstruction then provides a 2D photographic projection image of the optical properties given *a priori* information about the depth of the heterogeneity. Since the heterogeneity function (therefore the optical properties of the heterogeneities) is related to the scattered wave via the Weyl expansion of the Green's function, and since the amplitude and phase of the Weyl expansion depend upon the depth $z_d - z_j$, an incorrect depth estimate produces incorrect values of the reconstructed optical properties. This type of errors is intrinsic to the angular spectrum approach. However, rough estimation of the depth information can be tolerated if it is desirable to reconstruct contrast images of multiple objects.

Equation (22) reveals how the heterogeneity function and hence the reconstructed optical properties of the heterogeneities vary with the estimated depth. Choice of a too small depth underestimates the optical properties and a too large depth overestimates the optical properties. Figure 6(a) shows

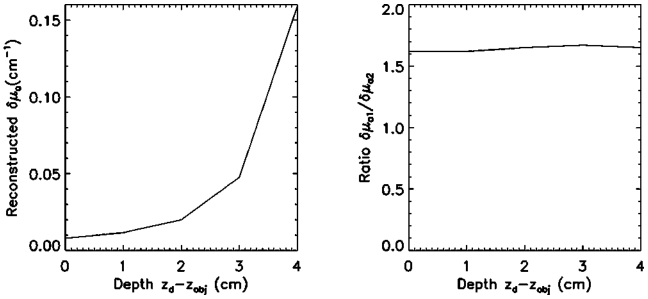

FIG. 6. (a) shows the reconstructed absorption coefficient versus the depth estimation. The data points in (a) are normalized by the absorption reconstructed at the depth where the object is, e.g., $z_d - z_{obj} = 2$ cm. (b) shows the ratio of reconstructed absorption of two spherical objects versus the depth estimation. Although the ratio is only approximately reconstructed (e.g., the true ratio is 2), the ratio is relatively insensitive to the depth estimate.

the reconstructed absorption coefficient of a spherical object versus the estimated depth $z_d - z_{obj}$. In this case, we have a spherical object of 0.5 cm radius 2 cm below the detection plane, i.e., $z_d - z_{obj} = 2$ cm. The true optical property variations of the spheres with respect to the background are $\delta\mu_a = 0.02\ \mathrm{cm}^{-1}$ and $\delta\mu_s' = 0$. We find that the reconstructed absorption increases as the estimated object depth increases. In Fig. 6(b), we plot the ratio of the reconstructed absorption coefficients of two spherical absorbing objects $(\delta\mu_{a1}^{rec}/\delta\mu_{a2}^{rec})$ versus the estimated depth. One sphere of $\delta\mu_{a1} = 0.04\ \mathrm{cm}^{-1}$ and $\delta\mu_{s1}' = 0\ \mathrm{cm}^{-1}$ is at (2, 1, 3) cm and the other sphere of $\delta\mu_{a2} = 0.02\ \mathrm{cm}^{-1}$ and $\delta\mu_{s2}' = 0\ \mathrm{cm}^{-1}$ is at (1,−1, 3) cm. Two spheres have the same size (0.5 cm in radius) and they are chosen to to be at the same depth, e.g., 2 cm below the detection plane. Therefore any depth estimate is either correct or incorrect for both objects at the same time, and we do not have to take into account the additional complexity shown in Fig. 6(a). We find that the ratio of the reconstructed absorption coefficients is not sensitive to the depth estimation, and therefore the incorrect depth estimate for contrast image can be tolerated in this case.

The image quality is also affected by the choice of *a priori* depth. Recall the heterogeneity function and the scattered wave in K space is coupled to each other via the Weyl expansion [see Eq. (22)]. The factor $e^{-im(z_d - z_{obj})}/m$ increases exponentially with the $(z_d - z_{obj})$. The noise (numerical and experimental) can be amplified at greater depths $(z_d - z_{obj})$. A series of reconstructed images with different depths are shown in Fig. 7. In this example an absorbing spherical object is at (2, 1, 3) cm and the scattered wave is measured in the plane at $z = 5$ cm over a $9\times 9\ \mathrm{cm}^2$ square with steps of 0.6 cm. The images (b)–(f) are reconstructed with assumptions of the depth $(z_d - z_{obj})$ to be respectively 4, 3, 2, 1, 0 cm. We find that the image quality gets worse (e.g., noisier) at greater depths. The depth-dependent noise and the *monotonic* variation of the image sharpness make it difficult to estimate the true object depth from image sharpness. For a spatially extended object, however, a choice of a shallow depth is often sufficient to reconstruct fairly well the spatial margins of inhomogeneities.

In order to obtain better 3D information with this diffraction tomography technique, one can use a secondary localization scheme to deduce the object depth. An example would be to scan the phased-array in two orthogonal planes [22,23]. Alternatively as shown in Fig. 8, if we take two planar measurements along two different directions of the same sample, the projection image 1 from the first measurement in one plane (plane 1) will provide the depth information for the projection image 2 from the second measurement in the other plane (plane 2).

D. Experimental results

To demonstrate the experimental feasibility of this algorithm, we have performed amplitude and phase measurements in a parallel-plane geometry (Fig. 2) within a tank filled with 50 liters 0.75% Intralipid $(\mu_{a0} = 0.020\ \mathrm{cm}^{-1}$, $\mu_{s0}' = 7.3\ \mathrm{cm}^{-1})$. We used a rapid homodyne detection sys-

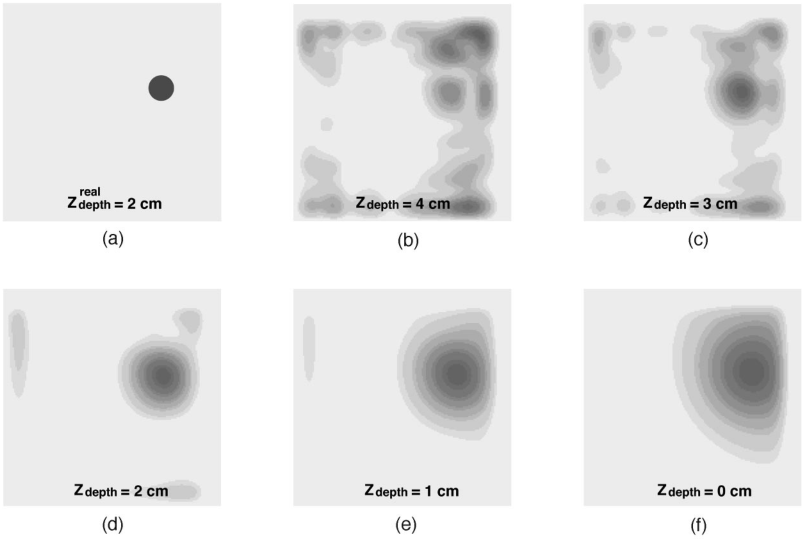

(a) (b) (c)

(d) (e) (f)

FIG. 7. Illustration of the dependence of reconstructed images on the estimated depth. The detection plane is at $z = 5$ cm and an absorbing object shown in (a) is at (2, 1, 3) cm, which is 2 cm below the detection plane. (b) through (f) are the images reconstructed with an estimated depth at, respectively, 4 cm, 3 cm, 2 cm, 1 cm, and 0 cm.

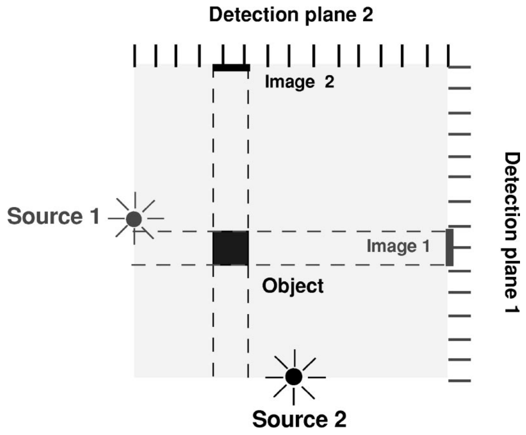

FIG. 8. Illustration of how to obtain a 3D image from two projection images reconstructed from two measurements along two orthogonal directions. Image 1 from the measurement in plane 1 provides the depth information for image 2 from the measurement in plane 2.

tem based upon in-phase/quadrature (IQ) demodulation techniques [20,24]. A block diagram and details of the experimental setup are given in reference [20].

The experimental geometry is shown in Fig. 2. The source position was fixed and taken to be the origin of our coordinate system. As shown in Fig. 2, we ''made'' the detection plane by scanning a single detection fiber over a square region from $(-4.65, -4.65, 5.0)$ cm to $(4.65, 4.65, 5.0)$ cm in a plane at $z_d = 5.0$ cm in steps of size $\Delta x = \Delta y = 0.3$ cm. The amplitude and phase of the DPDW was recorded at each position for a total of 1024 points. Each data point takes about half second. We directly measured the amplitude and phase in the *homogeneous* medium to obtain the background wave $\Phi_0(\mathbf{r_d})$.

In this experiment, an absorbing slice with dimensions $1.5\times1.5\times0.4$ cm^3 was submerged in the turbid medium (0.75% Intralipid) at position $(-1.6, -0.3, 3.0)$ cm. The slice was made of resin plus TiO_2 and absorbing dye. TiO_2 particles (from Sigma) cause the scattering and the absorbing dye (900NP from Zeneca) causes the absorption. The absorption coefficient of the slice was $\mu_{a,obj} = 0.12$ cm^{-1}; its scattering coefficient was about the same as that of the background, i.e., ~ 7.3 cm^{-1}. The scattered wave $\Phi_{sc}(\mathbf{r_d})$ was obtained by subtracting the background wave $\Phi_0(\mathbf{r_d})$ from the measured (total) signal $\Phi(\mathbf{r_d})$.

For image reconstruction, we first take the 2D Fourier transform of the scattered wave $\Phi_{sc}(\mathbf{r_d})$ measured at the detection plane $z = z_d$. Using Eq. (22) along with *a priori* information about the slice depth, we then obtain the heterogeneity function in K space $\hat{T}(p,q,z_{obj})$ in the plane containing the slice at $z = z_{obj}$. During this step, an ''m-cut'' filter is used to neglect high spatial frequency components with $\mathrm{Im}(m) > 3.5\,\mathrm{Im}(k_0)$ in the heterogeneity function $\hat{T}(p,q,z_{obj})$ [25]. We then take 2D inverse Fourier transform of $\hat{T}(p,q,z_{obj})$ with respect to spatial frequency (p,q) to obtain the heterogeneity function $T(x,y,z_{obj})$ in real space. Finally we divide the heterogeneity function $T(x,y,z_{obj})$ by the background field $\Phi_0(x,y,z_{obj})$ in the plane containing the slice at $z = z_{obj}$ to obtain a spatial map of the reconstructed absorption variation, e.g., $\delta\mu_a(x,y,z_{obj}) = T_{abs}(x,y,z_{obj})/[-v/D_0\Phi_0(x,y,z_{obj})]$. The homogeneous background field $\Phi_0(x,y,z_{obj})$ is calculated using the best estimated optical properties ($\mu_{a0} = 0.017$ cm^{-1} and $\mu'_{s0} = 7.21$ cm^{-1}) by fitting the background wave $\Phi_0(\mathbf{r_d})$ measured in the detection plane $z = z_d$ to the exact solution of DPDW's [e.g., $\Phi_0(\mathbf{r}) = vM_0 \exp(ik_0|\mathbf{r}-\mathbf{r}_s|)/4\pi D_0|\mathbf{r}-\mathbf{r}_s|$]. The reconstructed images of the slice are shown in Fig. 9. The complete reconstruction based upon forward and inverse FFT calculations takes less than 0.2 second CPU time on Sun Sparc10 workstation. The reconstructed x-y position was about at $(-1.80, -0.25)$ cm, close to the true x-y position at $(-1.6, -0.3)$ cm. Inaccuracies in the position measurements might account for the discrepancy. The reconstructed absorption coefficient is well above the background noise level and close to the true value, e.g., $\delta\mu^{rec}_{a,obj} = 0.125 \pm 0.018$ cm^{-1}. The uncertainty corresponds to 1 mm uncertainty in the slice depth estimation. Errors in our estimate of background optical properties, the refractive index mismatch between the object (~ 1.46) and background medium (~ 1.33) and our inability to detect high spatial frequency components in the scattered wave also contribute to the inaccuracy in reconstructed absorption properties.

VI. SIMULTANEOUS RECONSTRUCTION OF ABSORPTION AND SCATTERING, AND EXTRACTION OF BACKGROUND OPTICAL PROPERTIES

The angular spectrum algorithm provides an approximate relation between the heterogeneity function and the scattered

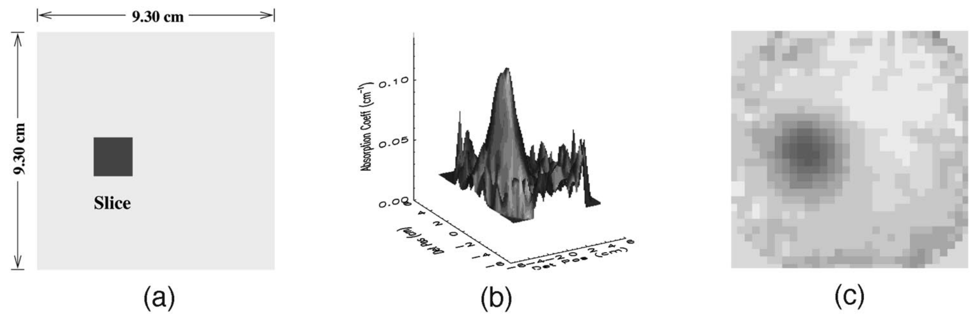

FIG. 9. (a) shows the exact x-y position of a thin absorbing slice. (b) shows the surface plot of the reconstructed absorption variation ($\delta\mu^{rec}_a$) using the angular spectrum algorithm. (c) illustrates the reconstructed 2D photographic image of this slice. Agreement between the reconstructed position and the exact position as shown in (a) can be readily found.

wave within the framework of the first order Born approximation. In addition to this first order approximation, it also requires knowledge of the background optical properties. The resultant images are 2D photographic-type images. In this section, we consider the possibility of simultaneous reconstruction of the absorption and scattering coefficients, and we explore methods to extract the background optical properties from a single measurement on a heterogeneous sample.

A. Absorption and scattering

So far, we have assumed that we have either purely absorbing inhomogeneities or purely scattering inhomogeneities, but not a mixture. We introduce a dual modulation frequency approach as a means to reconstruct the absorption and scattering coefficients simultaneously.

When both absorption and scattering variations are present, the heterogeneity function is

$$T(\mathbf{r})=-\frac{v}{D_0}\Phi_0(\mathbf{r})\,\delta\mu_a(\mathbf{r})+\frac{3D_0k_0^2}{v}\Phi_0(\mathbf{r})\,\delta\mu_s'(\mathbf{r}). \qquad (23)$$

Within a ‘‘thin’’ slice approximation, the heterogeneity function $T(\mathbf{r})$ in the plane at $z=z_{obj}$ can be obtained using the angular spectrum algorithm. Dividing $T(\mathbf{r})$ by the background wave $\Phi_0(\mathbf{r})$ in the plane at $z=z_{obj}$, we obtain the following quantity, denoted by $F(\omega)$, which is a function of $\delta\mu_a$, $\delta\mu_s'$, as well as the modulation frequency ω, i.e.,

$$F(\omega)=\left.\frac{T(\mathbf{r})}{\Phi_0(\mathbf{r})}\right|_{z_{obj}}=-3\mu_{s0}'\delta\mu_a(\mathbf{r})+\left[-3\mu_{a0}+i\frac{3\omega}{v}\right]\delta\mu_s'(\mathbf{r}). \qquad (24)$$

Note that the scattering variation $\delta\mu_s'$ appears along with the modulation frequency, while $\delta\mu_a$ does not. Therefore, if we measure the scattered wave at two different modulation frequencies ω_1 and ω_2, the difference between the two the reconstructed $F(\omega_1)$ and $F(\omega_2)$ will only be related to $\delta\mu_s'$:

$$F(\omega_2)-F(\omega_1)=i\frac{3(w_2-\omega_1)}{v}\,\delta\mu_s'. \qquad (25)$$

$\delta\mu_s'$ can be determined from Eq. (25). Then by substituting the resultant $\delta\mu_s'$ into Eq. (24), we can then determine the absorption variation $\delta\mu_a$.

To demonstrate the feasibility of this approach, we simultaneously reconstruct the absorption and scattering coefficients of a generic slice using simulated data. The simulation geometry is similar to the experimental geometry shown in Fig. 2. A $1\times1\times0.3\ \mathrm{cm}^3$ slice of $\mu_a=0.04\ \mathrm{cm}^{-1}$ and $\mu_s'=12.0\ \mathrm{cm}^{-1}$ is placed at $(1,-1,3)$ cm. The source is at $(0,0,0)$ cm and the homogeneous background has optical properties of $\mu_{a0}=0.02\ \mathrm{cm}^{-1}$ and $\mu_{s0}'=8.0\ \mathrm{cm}^{-1}$. Note that the slice has both absorption and scattering variations with respect to the homogeneous background. The total and background diffuse photon density waves at $z_d=5$ cm are calculated for $f=70$ MHz and $f=140$ MHz using the finite difference method. The reconstructed images are shown in Figs. 10(b) and 10(c). The reconstructed absorption and scattering coefficients are $\delta\mu_a=0.025\ \mathrm{cm}^{-1}$ and $\delta\mu_s'=3.32\ \mathrm{cm}^{-1}$. We find that this approach provides simultaneous estimates of the absorption and scattering coefficients with a reasonable accuracy.

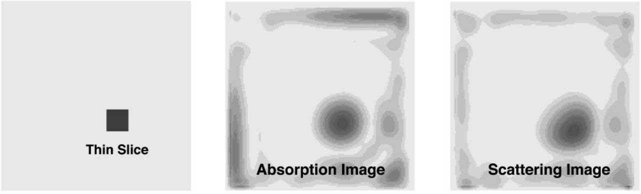

(a) (b) (c)

FIG. 10. (a) shows a thin slice object at (1, −1, 3) cm. The slice is 0.3 cm thick with its $1\times1\ \mathrm{cm}^2$ surface in parallel to the detection plane at $z_d=5$ cm. The scattered waves at two modulation frequencies (70 MHz and 140 MHz) in the detection plane at $z_d=5$ cm are calculated using finite difference method over a $9.3\times9.3\ \mathrm{cm}^2$ region with *x*-*y* steps of 0.3 cm. (b) and (c) show the absorption and scattering images reconstructed simultaneously using the dual modulation frequency approach. The reconstructed position of the slice is close to its true position and the reconstructed absorption and scattering properties are close to their true values. See Sec. VI A for details.

B. Extraction of background optical properties

Image reconstruction requires knowledge of the optical properties of the homogeneous background medium. For example, the complex spatial frequency $m=[k_0^2-(2\pi)^2(p^2+q^2)]^{1/2}$ in Eq. (22) depends on the background photon density wave number k_0, and k_0 in turn depends upon the absorption and scattering coefficients of the background turbid medium. It is derivable to determine the background optical properties from a single data set measured on a heterogeneous medium. One simple approach is to fit the heterogeneous data set with a homogeneous model and thus estimate the average values of the bulk optical properties. We find that the results by this approach are generally unsatisfactory. Figure 11(b) shows the total photon density wave $\Phi(\mathbf{r})$ (the amplitude, for example) from the absorbing slice experiment where the detector was scanned along a line symmetrically with respect to the source. When fitting all the data points with a simple homogeneous model, the resultant absorption and scattering coefficients are $\mu_{a0}^{fit}=0.012\ \mathrm{cm}^{-1}$ and $\mu_{s0}'^{fit}=6.27\ \mathrm{cm}^{-1}$, while the expected values for 0.75% Intralipid are $\mu_{a0}=0.020\ \mathrm{cm}^{-1}$ and $\mu_{s0}'=7.30\ \mathrm{cm}^{-1}$.

We can improve the results by considering the symmetry of our detection scheme. Our scanning geometry (see Fig. 2) is mirror symmetric with respect to the source. In Fig. 11(a), we project the 3D geometry into 2D to re-emphasize this mirror symmetry. If the medium is homogeneous, the data should be symmetric with respect to source; if the medium is heterogeneous, the left-right symmetry will be broken. This broken symmetry enables us to identify the data points that are substantially perturbed by the inhomogeneities. Since the phase of diffuse photon density waves is not as sensitive to the absorption variation as the amplitude, we use only the amplitudes of the photon density waves for identifying the most perturbed data points. If the left-right difference in amplitude signals is greater than the system noise level, we call

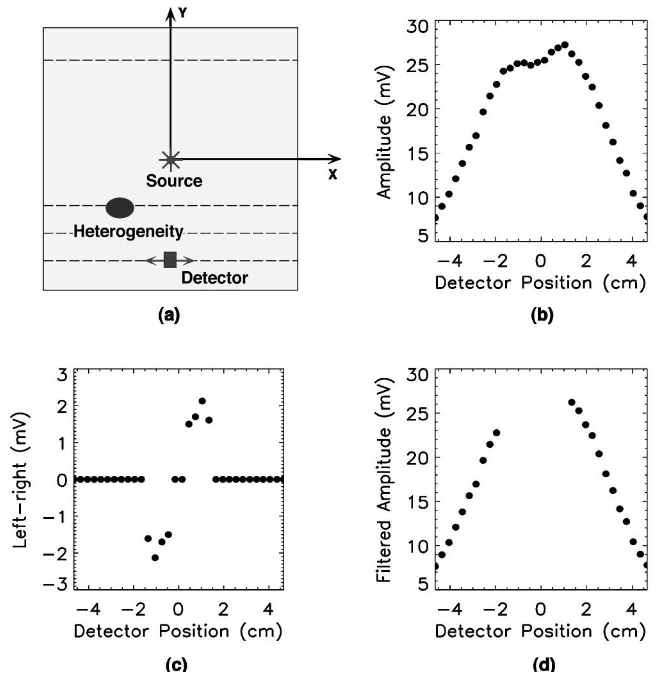

FIG. 11. (a) shows a 2D version of the experimental geometry in Fig. 2. The detector scans along a line from left to right symmetrically with respect to the source. (b) shows the raw data measured on a heterogeneous medium by scanning the detector along a line from left to right. (c) shows the most perturbed data points for which the left and right differences are greater than the noise level of our detection system (e.g., 2.5 mV in this case). (d) show the rest data points after the most perturbed data points are filtered out. The background optical properties can then be obtained by fitting the data points shown in (d) to a homogeneous model.

those data points the most perturbed data points [See Fig. 11(c)]. We then exclude these perturbed data points, and fit the rest of data points (both amplitude and phase) to a homogeneous model [see Fig. 11(d)]. We find that resultant optical properties are indeed improved, e.g., $\mu_{a0}^{fit}=0.015\ \mathrm{cm}^{-1}$ and $\mu_{s0}'^{fit}=7.23\ \mathrm{cm}^{-1}$. The inaccuracy decreases from $\sim 40\%$ to $\sim 25\%$ in μ_{a0} and from $\sim 18\%$ to $\sim 2\%$ in μ_{s0}'. This symmetry technique is similar to the phased-array technique in detection heterogeneities [23]. Although biological tissue is in general microscopically inhomogeneous, we speculate that this symmetry technique might work to a certain degrees for tissues with rather homogeneous macrostructures such as breast tissue. Further experimental investigations would be required to test the applicability of this technique to *in vivo* studies.

VII. SLAB AND SEMI-INFINITE GEOMETRIES

The total photon density wave $\Phi(\mathbf{r})$ for a turbid medium *with boundaries* was given by Eq. (13). On the surface of the turbid medium, the diffuse photon density wave satisfies the *zero partial current* boundary condition [26]

$$\Phi(\mathbf{r})+\frac{1+R_{eff}}{1-R_{eff}}\,\frac{2D_0}{v}\,\frac{\partial\Phi(\mathbf{r})}{\partial n'}=0\rightarrow\frac{\partial\Phi(\mathbf{r})}{\partial n'}=-\alpha\Phi(\mathbf{r}),\quad \text{for } \mathbf{r} \text{ on the surface.} \tag{26}$$

Here n' is the surface normal pointing outward from the scattering medium, $\alpha=[(1-R_{eff})/(1+R_{eff})]v/2D_0$ where R_{eff} is the effective reflection coefficient.[2] Using this zero partial current boundary condition in Eq. (13), we obtain a general solution for the total diffuse photon density wave $\Phi(\mathbf{r})$ in a finite turbid medium:

$$\Phi(\mathbf{r})=\frac{v}{D_0}\int_V S(\mathbf{r}')G(\mathbf{r},\mathbf{r}')d^3r'+\int_V T(\mathbf{r}')G(\mathbf{r},\mathbf{r}')d^3r' -\int_S \Phi(\mathbf{r}')\left[\alpha G(\mathbf{r},\mathbf{r}')+\frac{\partial G(\mathbf{r},\mathbf{r}')}{\partial n'}\right]dA'. \tag{27}$$

How is the scattered wave related to the heterogeneity function in this case? As we discussed at the end of Sec. III, the surface term depends on the total photon density wave $\Phi(\mathbf{r})$, and therefore the surface term includes both a background wave component and a scattered wave component. Analytic separation of the background wave component from the scattered wave component in the surface term is generally not feasible though perturbative approaches may be used approximately.

The approach we take here is to find an appropriate Green's function so that the surface term is zero by requiring

$$\alpha G(\mathbf{r},\mathbf{r}')+\frac{\partial G(\mathbf{r},\mathbf{r}')}{\partial n'}=0,\quad \mathbf{r} \text{ is on the surface.} \tag{28}$$

Note that this boundary condition, as we discussed in Sec. III, is naturally satisfied for an infinite turbid medium. By requiring the Green's function to satisfy Eq. (28), we then have the total photon density wave $\Phi(\mathbf{r})$:

$$\Phi(\mathbf{r})=\frac{v}{D_0}\int_V S(\mathbf{r}')G(\mathbf{r},\mathbf{r}')d^3r'+\int_V T(\mathbf{r}')G(\mathbf{r},\mathbf{r}')d^3r', \tag{29}$$

from which we can obtain the scattered wave $\Phi_{sc}(\mathbf{r})$

$$\Phi_{sc}(\mathbf{r})=\Phi(\mathbf{r})-\Phi_0(\mathbf{r})=\int_V T(\mathbf{r}')G(\mathbf{r},\mathbf{r}')d^3r'. \tag{30}$$

Our task is to find the appropriate Green's function which satisfies Eq. (12) and the boundary condition given by Eq. (28). We expect the Green's function for a finite medium to include the Green's function in an infinite medium $G_0(\mathbf{r},\mathbf{r}')$, and an additional term $G_h(\mathbf{r},\mathbf{r}')$ which results from backreflections at the boundaries, i.e.,

$$G(\mathbf{r},\mathbf{r}')=G_0(\mathbf{r},\mathbf{r}')+G_h(\mathbf{r},\mathbf{r}'), \tag{31}$$

---

[2] The exact expression of R_{eff} was derived by Haskell, Tromberg and their co-workers [26]. An approximate expression offered by Groenhuis and co-workers [27], is in agreement with the exact R_{eff} within 10%. The approximate expression is $R_{eff}=-1.440n^{-2}+0.710n^{-1}+0.668+0.0636n$ where the relative index of refraction $n=n_{in,turbid}/n_{out,air}$.

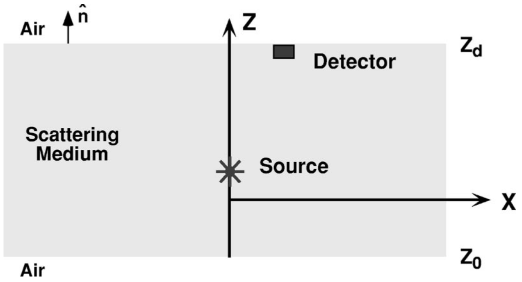

FIG. 12. A slab geometry is considered for the boundary problem. The slab is infinite long but has a finite thickness, e.g., $z_d - z_0$. One surface of the slab is at plane $z=z_0$ and another surface is at plane $z=z_d$. The turbid medium is between these two planes and outside the slab is nonscattering media such as air. This slab geometry is quite suitable for a compressed breast configuration in clinical studies.

where $G_0(\mathbf{r},\mathbf{r}')=\exp(ik_0|\mathbf{r}-\mathbf{r}'|)/4\pi|\mathbf{r}-\mathbf{r}'|$. $G_h(\mathbf{r},\mathbf{r}')$ is required to satisfy the homogeneous Helmholtz equation

$$(\nabla^2+k_0^2)G_h(\mathbf{r},\mathbf{r}')=0, \tag{32}$$

and the following boundary condition:

$$\alpha G_h(\mathbf{r},\mathbf{r}')+\frac{\partial G_h(\mathbf{r},\mathbf{r}')}{\partial n'}=-\left[\alpha G_0(\mathbf{r},\mathbf{r}')+\frac{\partial G_0(\mathbf{r},\mathbf{r}')}{\partial n'}\right], \quad \text{for } \mathbf{r} \text{ on the boundaries.} \tag{33}$$

A. Slab geometry

Boundaries of arbitrary shapes are, in general, difficult to incorporate into the solution of the photon diffusion equation [Eq. (13)]. Here, we consider a slab geometry shown in Fig. 12. Within the slab is the scattering medium and outside the slab is air. This slab geometry is to approximate the compressed breast configuration, which is suitable for clinical breast lesion diagnosis.

Suppose the two surfaces of a slab turbid medium are at $z=z_0$ and $z=z_d$ as shown in Fig. 12. Again we use the angular spectrum representation of the Green's function $G_h(\mathbf{r},\mathbf{r}')$, i.e.,

$$G_h(\mathbf{r},\mathbf{r}')=\int\int dp\,dq\,\hat{G}_h(p,q,z,z')e^{-i2\pi[p(x-x')+q(y-y')]}, \tag{34}$$

Substituting this equation in Eq. (32), we find for any given spatial frequencies (p,q), $\hat{G}_h(p,q,z,z')$ satisfies the following one-dimensional homogeneous Helmholtz equation:

$$\left[\frac{\partial^2}{\partial^2 z}+m^2\right]\hat{G}_h(p,q,z,z')=0, \tag{35}$$

where $m=[k_0^2-(2\pi)^2(p^2+q^2)]^{1/2}$ and $\mathrm{Im}(m)>0$. The boundary conditions given by Eq. (33) for a slab geometry shown in Fig. 12 can be rewritten for the angular spectrum $\hat{G}_h(p,q,z,z')$ as

$$\alpha\hat{G}_h(p,q,z,z'=z_0)-\frac{\partial\hat{G}_h(p,q,z,z'=z_0)}{\partial z'}=-(\alpha+im)\hat{G}_0(p,q,z,z'=z_0), \tag{36}$$

$$\alpha\hat{G}_h(p,q,z,z'=z_d)+\frac{\partial\hat{G}_h(p,q,z,z'=z_d)}{\partial z'}=-(\alpha+im)\hat{G}_0(p,q,z,z'=z_d), \tag{37}$$

where $\hat{G}_0(p,q,z,z')=(i/2m)e^{im|z-z'|}$ is given by the Weyl expansion [see Eq. (16)].

The general solution of $\hat{G}_h(p,q,z,z')$ has the form of

$$\hat{G}_h(p,q,z,z')=Ae^{imz'}+Be^{-imz'}. \tag{38}$$

The first term represents the wave which is reflected by the *lower* surface at $z=z_0$ and then propagates *forward* along $+z$ direction, i.e., the ''transmission'' component; the second term represents the wave which is reflected by the *upper* surface at $z=z_d$ and then propagates *backward* along $-z$ direction, i.e., the ''reflection'' component. Coefficients A and B can then be solved using the boundary conditions given by Eqs. (36) and (37). After some algebra, we find that

$$A=f_1e^{imz}+f_2e^{-imz}, \quad B=f_3e^{imz}+f_4e^{-imz}, \tag{39}$$

where f_1, f_2, f_3, and f_4 are given by

$$f_1=\frac{f_0}{\beta}(\alpha^2+m^2)e^{-im(z_d+z_0)},$$

$$f_2=-\frac{f_0}{\beta}(\alpha+im)^2e^{im(z_d-z_0)}, \tag{40}$$

$$f_3=-\frac{f_0}{\beta}(\alpha+im)^2e^{im(z_d-z_0)}, \quad f_4=\frac{f_0}{\beta}(\alpha^2+m^2)e^{im(z_d+z_0)}, \tag{41}$$

with

$$f_0=\frac{i}{2m}, \quad \beta=(\alpha+im)^2e^{im(z_d-z_0)}-(\alpha-im)^2e^{-im(z_d-z_0)}. \tag{42}$$

Finally, for a slab geometry, the Fourier component of total Green's function $\hat{G}(p,q,z,z')$ in K space is

$$\begin{aligned}\hat{G}(p,q,z,z')&=\hat{G}_0(p,q,z,z')+\hat{G}_h(p,q,z,z')\\&=f_0e^{im|z-z'|}+f_1e^{im(z+z')}+f_2e^{-im(z-z')}\\&\quad+f_3e^{im(z-z')}+f_4e^{-im(z+z')}.\end{aligned} \tag{43}$$

Using $\hat{G}(p,q,z,z')$, the relation between the scattered wave $\hat{\Phi}_{sc}(p,q,z_d)$ and the heterogeneity function $\hat{T}(p,q,z_{obj})$ for a slab geometry within ''thin'' slice approximation is

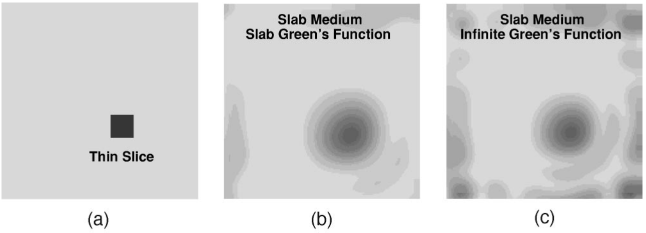

FIG. 13. (a) shows the position of a 0.3 cm thick, $1.0\times1.0\ \mathrm{cm}^2$ absorbing slice at (1, −1, 3) cm in a slab turbid medium. The two surfaces of the slab are respectively at planes $z=0$ cm and $z=5$ cm. The source is at origin at one of the slab surface ($z=0$ cm) and the detector scans at the other surface ($z=5$ cm). The reconstructed absorption image using the ''slab'' Green's function [Eq. (43)] is shown in (b). The reconstructed absorption image using the *wrong* ''infinite'' Green's function [Eq. (16)] is shown in (c).

$$\hat{T}(p,q,z_{obj})\approx\frac{\hat{\Phi}_{sc}(p,q,z_d)}{\Delta z\hat{G}(p,q,z_{obj})}. \tag{44}$$

The 2D inverse Fourier transform of $\hat{T}(p,q,z_{obj})$ gives the heterogeneity function $T(x,y,z_{obj})$ in real x-y space. The optical properties of the inhomogeneities can then be obtained, e.g., for absorbing objects, we have $\delta\mu_a(x,y,z_{obj})=T_{abs}(x,y,z_{obj})/[-v/D_0\Phi_0^{slab}(x,y,z_{obj})]$; and for scattering objects, we have $\delta\mu_s'(x,y,z_{obj})=T_{sc}(x,y,z_{obj})/[3D_0k_0^2/v\Phi_0^{slab}(x,y,z_{obj})]$.

Using the appropriate Green's function [Eq. (43)] for a slab geometry, we reconstructed a 2D optical image of a slice embedded in a slab turbid medium. The slab geometry is shown in Fig. 12 where the two surfaces are at planes $z=0$ and $z=5$ cm, respectively. The source is at the origin. A $1.0\times1.0\ \mathrm{cm}^2$ slice of 0.3 cm thick is at (1,−1,3) cm [see Fig. 13(a)] and the detection plane is at the top surface of the slab ($z=5$ cm). The slice has a higher absorption coefficient than the background medium but shares the same scattering coefficient with the background, e.g., $\mu_{aobj}=0.04\ \mathrm{cm}^{-1}$ and $\mu'_{sobj}=8.0\ \mathrm{cm}^{-1}$ for the slice and $\mu_{a0}=0.02\ \mathrm{cm}^{-1}$ and $\mu'_{s0}=8.0\ \mathrm{cm}^{-1}$ for the background. The total and background diffuse photon density waves at the top surface $z=5$ cm are calculated using the finite difference method.

The reconstructed absorption image using the appropriate Green's function [Eq. (43)] for the slab geometry is shown in Fig. 13(b), and the reconstructed absorption is $\delta\mu_{a,slab}^{rec}=0.0240\ \mathrm{cm}^{-1}$, which is close to the expected value $\delta\mu_a^{th}=0.0200\ \mathrm{cm}^{-1}$. For comparison, we also reconstructed the image of the slice using the *wrong* Green's function, i.e., the Green's $G_0(\mathbf{r},\mathbf{r}')$, which is only correct for the infinite medium [Eq. (16)]. The resultant absorption image is shown in Fig. 13(c). We found that the position of the slice can be well reconstructed by using different Green's functions. However the image shown in Fig. 13(c), which is reconstructed by using the *wrong* infinite Green's function, has more artifacts than that shown in Fig. 13(b), which is reconstructed by using the *right* slab Green's function. Notice that the Green's function for a slab geometry $|\hat{G}(p,q,z,z')|$ is smaller than the Green's function for an infinite geometry $|\hat{G}_0(p,q,z,z')|$ simply because we lose photons through the finite boundaries. When we use the Green's function of an infinite medium to reconstruct the image for a slab geometry, the overestimate of the Green's function is responsible for the nosier image structures (artifacts) in Fig. 13(c). The overestimated infinite Green's function also results in smaller reconstructed optical properties, e.g., the reconstructed value by using the *wrong* infinite Green's function, $\delta\mu_{a,wrong}^{rec}=0.0056\ \mathrm{cm}^{-1}$, is about 4 times as small as the value $\delta\mu_{a,slab}^{rec}=0.0240\ \mathrm{cm}^{-1}$ reconstructed by using the appropriate slab Green's function. We see that the appropriate Green's function for a slab geometry [Eq. (43)] produces cleaner images and more accurate optical properties than the Green's function which is only suitable for an infinite medium [Eq. (16)].

B. Semi-infinite geometry

As an extension of the above derivation, we can easily obtain the Fourier component of the total Green's function $\hat{G}^{semi}(p,q,z,z')$ for a *semi-infinite* turbid medium. Alternatively we can start with the Green's function for a slab geometry [Eq. (43)], then move the lower boundary of the slab in Fig. 12 to the negative infinity, i.e., $z_0\rightarrow-\infty$. Note that $\mathrm{Im}(m)>0$ and therefore all terms in Eq. (43) with e^{-imz_0} vanish when $z_0\rightarrow-\infty$. The Fourier component of the total Green's function $\hat{G}^{semi}(p,q,z,z')$ for a *semi-infinite* medium at any spatial frequencies (p,q) in K space is thus

$$\hat{G}^{semi}(p,q,z,z')=f_0e^{im|z-z'|}+f_4^{semi}e^{-im(z+z')}. \tag{45}$$

Here, the coefficients f_0 and f_4^{semi} are given by

$$f_0=\frac{i}{2m},\quad f_4^{semi}=-f_0\frac{\alpha+im}{\alpha-im}e^{2imz_d}. \tag{46}$$

The first term on the right hand side of Eq. (45) represents the Green's function in an infinite medium, and the second term represents the wave, which is reflected by the boundary at $z=z_d$ and propagates backward along the negative z direction. For arbitrary boundaries the solution of the Green's function are in general difficult to obtain.

C. Re-emission geometry

In the preceding discussions the source and the detector were assumed to be on the opposite sides of the inhomogeneity. This configuration is called transmission [see Fig. 14(a)]. It is suitable for two-plate soft compression geometry in breast cancer studies, with the source placed on one plate and the detector scanned over the other plate. Interestingly, the derivation is not limited to this transmission configuration. Recall that dependence of the angular spectrum algorithm on the source position is implied in the heterogeneity function [see Eqs. (10) and (11)]. The relation between the heterogeneity function and the scattered wave measured at the detection plane [see Eq. (22)] does not explicitly depend on the source position. The light source and the detector can be placed on the same side or on the opposite sides of the object without affecting the conclusion of the above derivation. Hence, we can apply the algorithm equally well to another geometry–the re-emission geometry [see Fig. 14(b)]

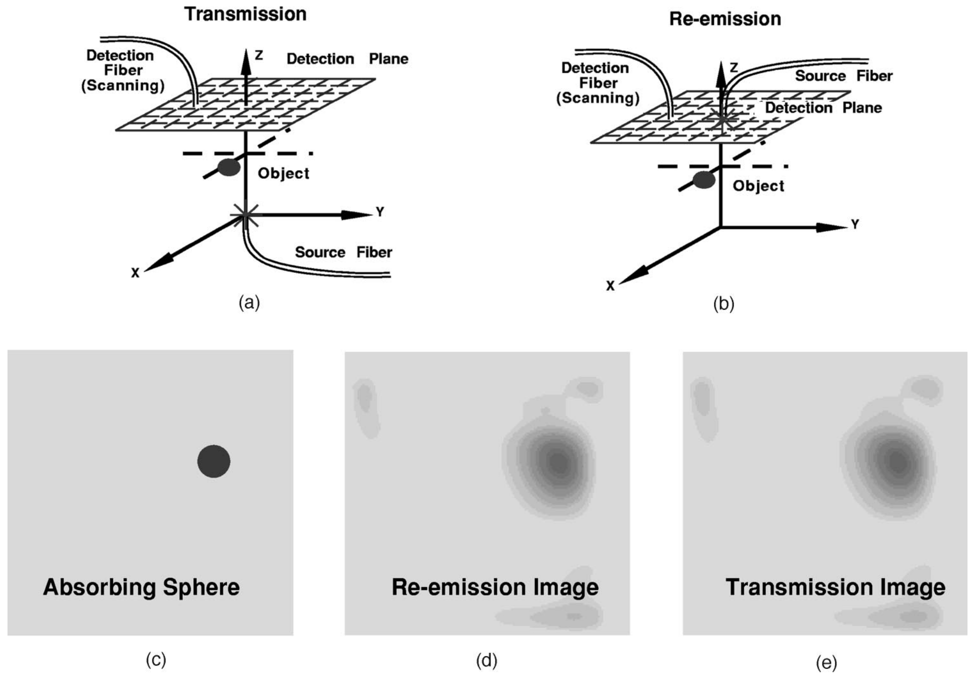

FIG. 14. (a) shows the transmission geometry. The source is at the origin and the detector scans in a plane at $z=z_d$. (b) shows the re-emission geometry where the source is at the center of the detection plane at $z=z_d$. (c) illustrates a spherical absorbing object at (2, 1, 2) cm embedded within a slab turbid medium. The two surfaces of the slab are at $z_0=0$ cm and $z_d=4.0$ cm, respectively. For both transmission and re-emission geometries, the scattered waves in the detection plane at $z_d=4$ cm are calculated using the exact DPDW solution for a slab geometry over a 9×9 cm^2 region with x-y steps of 0.6 cm. The reconstructed images for the re-emission and transmission geometries are shown in (d) and (e), respectively. The two images look similar. We also found that the reconstructed absorption coefficients are also about the same under both geometries.

[28,29]. In the re-emission configuration, the detector scans in the plane which contains the source. This could be necessary, for example, in brain function studies. The re-emission geometry could also be useful for studies of large dense breast tissues in which fewer photons pass through the tissue.

In the transmission geometry, we measure the scattered wave propagating *forward* away from the source; in the re-emission geometry, we measure the scattered wave propagating *backward* towards the source. For a re-emission geometry and within a thin slice approximation, the relation of the heterogeneity function $\hat{T}(p,q,z_{obj})$ in K space with the measured scattered wave in the plane $z=z_d$ is given by the same equation as for the transmission geometry [Eq. (22)]. Here, we rewrite the relation for the re-emission geometry:

$$\hat{T}(p,q,z_{obj})=\frac{\hat{\Phi}_{sc}(p,q,z_d)}{\Delta z\hat{G}(p,q,z_d,z_{obj})}, \tag{47}$$

where an appropriate Green's function for an infinite medium [Eq. (16)] or a slab medium [Eq. (43)] has been assumed.

Simulations have shown the applicability of the algorithm to the re-emission geometry. Consider an absorbing spherical inhomogeneity of 0.5 cm radius at (2, 1, 2) cm embedded in an otherwise homogeneous slab turbid medium [see Fig. 14(c)]. The two surfaces of the slab are at $z_0=0$ cm and $z_d=4.0$ cm, respectively. The absorption and scattering coefficients of the sphere are $\mu_a=0.04$ cm^{-1} and $\mu_s'=8.0$ cm^{-1} while the background optical properties are $\mu_{a0}=0.02$ cm^{-1} and $\mu_{s0}'=8.0$ cm^{-1}. For the re-emission configuration, both the source and detector are placed on the top surface of the slab, i.e., in a plane at $z_d=4$ cm. The scattered wave is calculated over a 9×9 cm^2 region with x-y steps of 0.6 cm. The source is placed at the center of the square scanning region in the detection plane, i.e., at (0, 0, 4) cm. The reconstructed image for the re-emission geometry is shown in Fig. 14(d). For comparison we also reconstruct the image of the same object for the transmission geometry. In this case the source is at the origin (0, 0, 0) cm, on the lower surface of the slab, with all other configurations kept the same as in the re-emission geometry. The image is shown in Fig. 14(e). We see that the image quality in these two configurations is about the same. The ratio of the reconstructed absorption coefficient for the re-emission geometry to that for the transmission geometry is $\delta\mu_{a,re-em}^{rec}/\delta\mu_{a,trans}^{rec}\sim 1.1$. The finite object size (as opposed to a ''thin'' slice) might contribute to the small difference in the reconstructed absorption.

VIII. SUMMARY

We have presented a full exposition of our recent work that employs the angular spectrum algorithm for optical diffraction tomography with diffuse photon density waves. The image reconstruction becomes practically easy for thin heterogeneities wherein the heterogeneity function of interest is proportional to the scattered wave measured at the detection plane, i.e., $\hat{T}(p,q,z_{obj})\propto\Phi_{sc}(p,q,z_d)$. We have shown that although this relation is accurate only for thin inhomogeneities, it provides an approximate short cut for fast, 2D projection imaging of spatially extended objects. The reconstruction is very rapid, requiring only a forward and inverse Fourier transform, e.g., it takes less than 0.2 second on a Sparc10 workstation to reconstruct an image of ~1000 pixels. For spatially extended objects, although the reconstructed optical properties are not accurate, the ratio of the reconstructed optical properties of multiple objects are close to the true ratio. In this sense we say that *contrast* image can still be obtained by using this algorithm. The feasibility for using this algorithm for image reconstruction of absorbing and scattering inhomogeneities has been experimentally demonstrated [20]. We have also shown that the absorption and scattering properties can be reconstructed simultaneously using the angular spectrum algorithm with scattered wave measured at two different modulation frequencies. Authors perceive that the angular spectrum algorithm could potentially apply for breast cancer imaging given that boundary matching is employed to reduce the boundary effect [30]. The method could also be used for differential imaging of the preferential accumulation of an exogenous contrast agent in biological tissues [31].

We have extended the theory to other geometries including the slab and the semi-infinite geometry for both transmission and re-emission configuration. The theory was confirmed in simulation experiments.

ACKNOWLEDGMENTS

We gratefully acknowledge technical discussion with Cecil Cheung and assistance from Monica Holboke with finite difference calculations. This research was supported by the National Institutes of Health under Grant Nos. R01-CA75124 (A.G.Y.) and R-01-CA72895 (B.C.), and by the U.S. Army under Grant No. DAMD17-97-1-7272 (A.G.Y.).

APPENDIX A: CONVENTIONS USED IN THIS PAPER REGARDING FOURIER TRANSFORM

The conventions regarding the forward and inverse Fourier transforms are as follows. Consider a function $f(x)$ in one dimension:

Forward Fourier transform:

$$F(p)=\int f(x)e^{i2\pi xp}dx; \tag{A1}$$

Inverse Fourier transform:

$$f(x)=\int F(q)e^{-i2\pi xp}dp; \tag{A2}$$

and the δ function is therefore given by

$$\delta(p)=\int e^{i2\pi xp}dx, \quad \delta(x)=\int e^{-i2\pi px}dp. \tag{A3}$$

Using these conventions, we eliminate the 2π factor outside the integral of forward and inverse Fourier transforms.

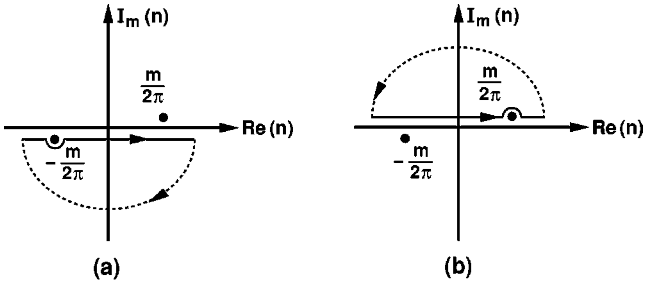

FIG. 15. There are two poles for the integral over n in Eq. (B6). (a): for $z>0$ the singularity is at $n=-m/2\pi$ and the integral is done along the lower close curve; (b): for $z<0$ the singularity is at $n=m/2\pi$ and the integral is done along the upper close curve.

APPENDIX B: THE WEYL EXPANSION OF GREEN'S FUNCTION

Consider an infinite turbid medium. μ_{a0} and μ_{s0}' are respectively the absorption and scattering coefficients. The Green's function $G_0(\mathbf{r},\mathbf{r}')$ satisfies the following equation:

$$(\nabla^2+k_0^2)G_0(\mathbf{r},\mathbf{r}')=-\delta(\mathbf{r},\mathbf{r}'), \tag{B1}$$

where $k_0=[(-v\mu_{a0}+i\omega)/D_0]^{1/2}$ with $\mathrm{Im}(k_0)>0$; $D_0=v/(3\mu_{s0}')$ is the photon diffusion coefficient. The solution of the Green's function is [32]

$$G_0(\mathbf{r},\mathbf{r}')=\frac{e^{ik_0|\mathbf{r}-\mathbf{r}'|}}{4\pi|\mathbf{r}-\mathbf{r}'|}. \tag{B2}$$

The Green's function is related to its Fourier transform by

$$G_0(\mathbf{r})=\int\int\int \hat{G}_0(p,q,n)e^{-i2\pi(px+qy+nz)}dp\,dq\,dn, \tag{B3}$$

where we assume $\mathbf{r}'=0$ without losing generality and (p,q,n) are the spatial frequencies. Plugging Eq. (B3) into Eq. (B2) and using the integral expression for the δ function [Eq. (A3)], we have

$$\begin{aligned}\int\int\int &\hat{G}_0(p,q,n)[k_0^2-(2\pi)^2(p^2+q^2+n^2)]\\ &\times e^{-i2\pi(px+qy+nz)}dp\,dq\,dn\\ =-&\int\int\int e^{-i2\pi(px+qy+nz)}dp\,dq\,dn.\end{aligned} \tag{B4}$$

Without a rigorous proof, we can obtain the Fourier transform of the Green's function just by looking at both sides of the above equation, i.e.,

$$\hat{G}_0(p,q,n)=\frac{1}{(2\pi)^2(p^2+q^2+n^2)-k_0^2}=\frac{1}{(2\pi)^2n^2-m^2}, \tag{B5}$$

where $m=[k_0^2-(2\pi)^2(p^2+q^2)]^{1/2}$ and $\mathrm{Im}(m)>0$. Eq. (B3) can then written as

$$G_0(\mathbf{r})=\int\int dp\,dq\,e^{-i2\pi(px+qy)}\int\frac{e^{-i2\pi nz}}{(2\pi)^2n^2-m^2}dn, \tag{B6}$$

The integral over spatial frequency n can first be done by ''pole'' structure analysis. There are two poles in the integral over n as shown in Fig. 15. For $z>0$, we require $\mathrm{Im}(n)<0$ to ensure the convergence of the integral over n. Therefore, we choose the pole in the lower half space [Fig. 15(a)], e.g., $n=-m/2\pi$ [recall $\mathrm{Im}(m)>0$, which gives $\mathrm{Im}(n)<0$]. Note that the integral is along the clockwise direction which gives us an extra minus sign. The resultant integral is

$$\int \frac{e^{-i2\pi nz}}{(2\pi)^2\left(n+\frac{m}{2\pi}\right)\left(n-\frac{m}{2\pi}\right)}dn=-2\pi i\,\frac{e^{-i2\pi nz}}{(2\pi)^2\left(n-\frac{m}{2\pi}\right)}\overset{n=-m/2\pi}{=}\frac{i}{2m}e^{imz}. \tag{B7}$$

Similarly, for $z<0$ we require $\mathrm{Im}(n)>0$. Therefore we choose the pole in the upper half space [Fig. 15(b)], e.g., $n=m/2\pi$. The integral is along the counter-clockwise direction so there is no extra minus sign in this case. The resultant integral is thus

$$\int \frac{e^{-i2\pi nz}}{(2\pi)^2\left(n+\frac{m}{2\pi}\right)\left(n-\frac{m}{2\pi}\right)}dn=2\pi i\frac{e^{-i2\pi nz}}{(2\pi)^2\left(n+\frac{m}{2\pi}\right)}\overset{n=m/2\pi}{=}\frac{i}{2m}e^{-imz}. \tag{B8}$$

Combining Eqs. (B7) and (B8), we have the general expression for the integral over n:

$$\int \frac{e^{-i2\pi nz}}{(2\pi)^2n^2-m^2}dn=\frac{i}{2m}e^{im|z|}. \tag{B9}$$

Substituting this equation into Eq. (B6), we then end up with the Weyl expansion of the Green's function:

$$G_0(\mathbf{r})=\int\int dp\,dq\,e^{-i2\pi(px+qy)}\frac{i}{2m}e^{im|z|}, \tag{B10}$$

where $m=[k_0^2-(2\pi)^2(p^2+q^2)]^{1/2}$ and $\mathrm{Im}(m)>0$.

The Weyl expansion represents the superposition of elementary harmonic waves in the x and y directions ($e^{-i2\pi(px+qy)}$); the harmonic waves exponentially attenuate in the z direction away from the plane $z=0$ which contains the source. The harmonic waves and the attenuation factor $ie^{im|z|}/2m$ are so combined that the double integral in Eq. (B10) over all the spatial frequencies (p,q) yields the elementary damped spherical wave on the left-hand side of Eq. (B10), i.e., $G_0(\mathbf{r})=e^{ik_0r}/(4\pi r)$.

[1] M. Cutler, Surg. Gynecol. Obstet. **48**, 721 (1929).
[2] A. Yodh and B. Chance, Phys. Today **48** (3), 34 (1995).
[3] C. C. Johnson, IEEE Trans. Biomed. Eng. **17**, 129 (1970).
[4] A. Ishimaru, *Wave Propagation and Scattering in Random Media* (Academic Press, New York, 1978).
[5] M. S. Patterson, B. Chance, and B. C. Wilson, Appl. Opt. **28**, 2331 (1989).
[6] E. Gratton *et al.*, in *Proceedings of the Third International Conference for Peace Through Mind/Brain Science, Hamamatsu City, 1999*, edited by B. Chance (Hamamatsu Photonics K.K., 1990).
[7] J. B. Fishkin and E. Gratton, J. Opt. Soc. Am. A **10**, 127 (Jan 1993).
[8] J. B. Fishkin *et al.*, Appl. Opt. **36**, 10 (1997).
[9] *Advances in Optical Imagning and Photon Migration*, Volume XXI of *Trends in Optics and Photonics*, edited by J. G. Fujimoto and M. S. Patterson (Optical Society of America, Orlando, 1998).
[10] M. A. O'Leary, D. A. Boas, B. Chance, and A. G. Yodh, Opt. Lett. **20**, 426 (1995).
[11] S. R. Arridge, M. Schweiger, M. Hiraoka, and D. T. Delpy, SPIE Proc. **1888**, 360 (1993).
[12] B. W. Pogue, M. S. Patterson, H. Jiang, and K. D. Paulsen, Phys. Med. Biol. **40**, 1709 (1995).
[13] H. Jiang *et al.*, Opt. Lett. **20**, 2128 (1995).
[14] J. H. Chang, H. L. Graber, and R. L. Barbour, IEEE Trans. Biomed. Eng. **44**, 810 (1997).
[15] C. P. Gonatas, M. Ishii, J. S. Leigh, and J. C. Schotland, Phys. Rev. E **52**, 4361 (1995).
[16] E. Wolf, Opt. Commun. **1**, 153 (1969).
[17] D. N. Pattanayak, GE Tech. Info. Series 91CRD241, (1991).
[18] C. L. Matson and H. L. Liu, J. Opt. Soc. Am. A **16**, 1254 (1999).
[19] B. Q. Chen, J. J. Stamnes, and K. Stamnes, Pure Appl. Opt. **7**, 1161 (1998).
[20] X. D. Li *et al.*, Opt. Lett. **22**, 573 (1997).
[21] A. J. Banos, in *Dipole Radiation in the Presence of a Conducting Half-Space* (Pergamon Press, New York, 1966).
[22] B. Chance *et al.*, Proc. Natl. Acad. Sci. USA **90**, 3423 (1993).
[23] B. Chance *et al.*, Rev. Sci. Instrum. **67**, 4324 (1996).
[24] Y. S. Yang, H. L. Liu, X. D. Li, and B. Chance, Opt. Eng. **36**, 1562 (1997).
[25] T. Durduran *et al.*, Opt. Express **4**, 247 (1999).
[26] R. C. Haskell *et al.*, J. Opt. Soc. Am. A **11**, 2727 (1994).
[27] R. A. J. Groenhuis, H. A. Ferwerda, and J. J. T. Bosch, Appl. Opt. **22**, 2456 (1983).
[28] X. D. Li, Ph.D. thesis, University of Pennsylvania, 1998.
[29] X. Cheng and D. Boas, Opt. Express **3**, 118 (1998).
[30] X. D. Li *et al.*, Tech. Dig. Ser.-CLEO'98 **6**, 88 (1998).
[31] V. Ntziachristos, B. Chance, and A. G. Yodh, Opt. Express **5**, 230 (1999).
[32] J. D. Jackson, in *Classical Electrodynamics* (Wiley and Sons Inc., New York, 1975).